

Contributions of Downstream Eddy Development to the Teleconnection between ENSO and the Atmospheric Circulation over the North Atlantic

YING LI*

Program in Atmospheric and Oceanic Sciences, Princeton University, Princeton, New Jersey

NGAR-CHEUNG LAU

NOAA/Geophysical Fluid Dynamics Laboratory, Princeton, New Jersey

(Manuscript received 7 July 2011, in final form 16 December 2011)

ABSTRACT

The spatiotemporal evolution of various meteorological phenomena associated with El Niño–Southern Oscillation (ENSO) in the North Pacific–North American–North Atlantic sector is examined using both NCEP–NCAR reanalyses and output from a 2000-yr integration of a global coupled climate model. Particular attention is devoted to the implications of downstream eddy developments on the relationship between ENSO and the atmospheric circulation over the North Atlantic.

The El Niño-related persistent events are characterized by a strengthened Pacific subtropical jet stream and an equatorward-shifted storm track over the North Pacific. The wave packets that populate the storm tracks travel eastward through downstream development. The barotropic forcing of the embedded synoptic-scale eddies is conducive to the formation of a flow that resembles the negative phase of the North Atlantic Oscillation (NAO). The more frequent and higher persistence of those episodes during El Niño winters contribute to the prevalence of negative NAO conditions.

The above processes are further delineated by conducting a case study for the 2009/10 winter season, in which both El Niño and negative NAO conditions prevailed. It is illustrated that the frequent and intense surface cyclone development over North America and the western Atlantic throughout that winter are associated with upper-level troughs propagating across North America, which in turn are linked to downstream evolution of wave packets originating from the Pacific storm track.

1. Introduction

The El Niño–Southern Oscillation (ENSO) is the dominant mechanism contributing to interannual climate variability and has strong influences on the global atmospheric circulation (e.g., Bjerknes 1969; Trenberth et al. 1998). The impacts of ENSO on the midlatitude flow pattern are most discernible over the North Pacific (NP) and North American region (Horel and Wallace 1981). However, Nigam (2003, see his Fig. 14) has noted that the spatial structure of ENSO-related geopotential height

anomalies is distinct from the typical Pacific–North American (PNA) pattern.

More recently, a possible link between ENSO and North Atlantic–European climate has been noted on the basis of both observational data (Fraedrich and Müller 1992; Dong et al. 2000; Moron and Gouirand 2003; Pozo-Vázquez et al. 2001, 2005; Brönnimann et al. 2004, 2007) and numerical experiments (Merkel and Latif 2002; Mathieu et al. 2004; Ineson and Scaife 2009). In particular, negative phase of the North Atlantic Oscillation (NAO) has a high incidence in late winter El Niño events, whereas positive phase of NAO occurs more frequently in La Niña episodes. Recently, the dynamical mechanism for the late winter teleconnection between ENSO and NAO is examined in Li and Lau (2012, hereafter LL12) using mostly composites of seasonal means. By analyzing the output from a 2000-yr-long coupled atmosphere–ocean general circulation model (GCM), and by performing parallel analysis of observations and experiments

* Current affiliation: Department of Atmospheric Science, Colorado State University, Fort Collins, Colorado.

Corresponding author address: Ying Li, Department of Atmospheric Science, Colorado State University, 3915 W. Laporte Ave., Fort Collins, CO 80523.
E-mail: yingli@atmos.colostate.edu

with an atmospheric GCM, these investigators have explicitly shown the potential role of high-frequency transient eddies in the above teleconnection. During El Niño winters, the intensified transient disturbances along the equatorward-shifted NP storm track extend their influences farther downstream, thereby leading to an eastward extension of eddy vorticity forcing to the North Atlantic (NA) region. Such eddy forcing induces negative geopotential height tendencies along the southern lobe of the NAO, so that the anomalous flow pattern resembles that associated with the negative phase of the NAO. The opposite situation prevails in La Niña winters.

Many observational studies have shown that a substantial fraction of low-frequency variability is related to the behavior of large-scale persistent and recurrent flow patterns. Some investigations have referred to these features as weather regimes (e.g., Vautard 1990). Notable examples of such phenomena include blocking events and episodes with strong zonal flows (e.g., Dole and Gordon 1983). The characteristic time scales of persistent anomalies over NP, NA, and Siberia are estimated to be on the order of 10–15 days (Dole 1986; Feldstein 2000). Since the analysis performed in LL12 is mostly based on averages over two entire calendar months in late winter, the results presented in that study may be viewed as the crude average over several life cycles of such anomalous episodes. In those instances when episodes of both polarities occur within a given two-month period, or when the episodes are interspersed with extended periods with weak anomalies, the previous computations based on two-month averages might not yield optimal information on the processes associated with episodes of a given sign. In the present study, an attempt is made to sharpen the analysis approach in LL12 by focusing only on those periods when the episodes of interest attain sufficiently large amplitudes.

The influences of upstream seeding of transient disturbances from the eastern Pacific on the NAO phase have been noted in several studies. Franzke et al. (2004) point out that the initial latitudinal position of the Pacific storm track is essential for determining the NAO phase. Rivière and Orlanski (2007) also emphasize that waves originating from the eastern Pacific and traveling through the Atlantic domain play an important role in determining the phase of the NAO. Given the meridional shift and eastward extension of the Pacific storm track during ENSO events (e.g., Hoerling and Ting 1994; Straus and Shukla 1997; Chang 1998; Zhang and Held 1999; Seager et al. 2003; Lau et al. 2005; Orlanski 2005; LL12), it is anticipated that a link exists between ENSO and the NAO through downstream eddy propagation from NP to NA.

The term “downstream development” is often used to describe the successive appearance of troughs and ridges

downstream from an existing trough or ridge. This behavior is particularly noticeable in the wave packets that populate the storm tracks and is associated with the dispersive character of baroclinic eddies embedded therein. There are numerous modeling and observational studies on downstream development and wave packets (e.g., Simmons and Hoskins 1979; Chang 1993). The climatological aspects of these features are well documented (e.g., Chang and Yu 1999; Chang 1999). While the seasonal statistics, as shown in LL12, suggest a strengthened linkage between NP and NA storm tracks during ENSO winters, that study does not provide explicit evidence on the propagation of individual eddies from NP to NA. In this paper, we analyze the daily data from the same coupled GCM run as well as from observational archives, to illustrate the downstream development of the wave packets in the course of identified persistent episodes and the effects of subsequent barotropic eddy forcing on the slowly varying flow pattern over NA.

The 2009/10 winter is noted for the storminess over North America. El Niño and strong negative NAO conditions also prevailed in this period. We are hence motivated to perform a case study on the role of transient disturbances in the linkage between ENSO and NAO in this particular winter season, and to examine the implications of this relationship on the surface weather over North America.

The basic datasets, analysis tools, and procedure for the selection of persistent events are described in section 2. Section 3 documents the relationships between the frequency of occurrence of persistent events, ENSO and NAO. The characteristics of the eddy intensity, eddy propagation, and eddy-induced geopotential height tendencies during both phases of the persistent events are discussed in section 4. Section 5 shows the downstream development of the wave packets in the course of both phases of the selected persistent events. Results on surface cyclone development, downstream evolution of wave packets, and eddy forcing over NA, all for the outstanding winter season of 2009/10, are presented in section 6. Discussion and conclusions are given in section 7.

2. Data and analysis procedures

a. Model description

The model data analyzed in this study are generated by a 2000-yr-long preindustrial control simulation using the global Geophysical Fluid Dynamics Laboratory Climate Model version 2.1 (GFDL CM2.1; see Delworth et al. 2006; Gnanadesikan et al. 2006; Griffies et al. 2004). Readers are referred to LL12 for more detailed

descriptions of this model simulation. As shown in LL12, this model captures many salient features of the observed behavior of both ENSO and NAO as well as their impacts on the surface climate in late winter.

b. Observational datasets

The observed data used in this study are based on daily averaged fields (1948–present) from National Centers for Environmental Prediction (NCEP)–National Center for Atmospheric Research (NCAR) reanalysis (Kalnay et al. 1996). Six-hourly circulation fields in the 2009/10 winter season are used in the case study presented in section 6. December–February (DJF)-mean Niño-3 index (SST anomalies averaged over 5°S–5°N, 150°–90°W) based on the National Oceanic and Atmospheric Administration (NOAA) extended reconstructed SST version 3 dataset (ERSST V3, see Smith et al. 2008; Xue et al. 2003), is used to describe ENSO variability in the 1948–2010 period.

The geopotential height and sea level pressure (SLP) fields are multiplied by the factor [$\sin 45^\circ\text{N}/\sin(\text{latitude})$] to obtain streamfunction-like anomalies, which are better indicators of the associated wind and vorticity anomalies (Dole and Gordon 1983; Nakamura and Wallace 1990).

c. Analysis tool

A Lanczos 2–8-day bandpass filter with 41 weights (Duchon 1979) is used to retain high-frequency variability associated with baroclinic waves. Another 8-day low-pass filter is employed to capture the low-frequency circulation anomalies, which may be regarded as the background state for the high-frequency eddies. Nakamura et al. (2002) and Nakamura and Shimpo (2004) have used the same cutoff period of 8 days to separate the fluctuations in the two frequency bands. This cutoff period is slightly shorter than the 10-day cutoff used in LL12, to reduce the impact of the low-pass filtering on the selection of persistent events (see section 2d).

As in LL12, the characteristics of transient eddies are illustrated by using an index of storm-track activity, extended Eliassen–Palm vectors (hereafter referred to as \mathbf{E}), and the barotropic component of eddy forcing. The main distinction between the analysis approach in LL12 and the present study is that the previous investigation is based on monthly or seasonal averages of these diagnostic quantities, whereas the current work makes use of the same quantities defined on individual days.

A measure of the level of eddy activity on each day is given by the “envelope function” (Z_e) as defined by Nakamura and Wallace (1990):

$$\sqrt{2 \times \overline{Z'^2}} [\sin(45^\circ\text{N})/\sin(\text{latitude})].$$

Here the prime denotes the 2–8-day bandpass-filtered geopotential height, and overbar the smoothing with 8-day low-pass filter.

The horizontal components of \mathbf{E} for each day are given by Trenberth (1986):

$$\frac{1}{2} (\overline{v'^2} - \overline{u'^2}) \mathbf{i} - \overline{u'v'} \mathbf{j}.$$

Here u and v are the zonal and meridional wind components, respectively. Primes and overbars have the same meaning as in the definition of the envelope function above.

The daily fields of the low-pass-filtered tendency of the 250-hPa geopotential height, as induced by the convergence of transient eddy vorticity flux, are computed as (Nakamura et al. 1997):

$$\left(\frac{\partial Z_{250}}{\partial t} \right)_{\text{eddy}} = \frac{f_0}{g} \nabla^{-2} [-\nabla \cdot (\overline{\mathbf{V}'\zeta'})]. \quad (1)$$

Here Z_{250} is the geopotential height at 250 hPa, \mathbf{V} the horizontal wind, ζ the relative vorticity, f_0 the Coriolis parameter at 45°N, and g the acceleration due to gravity. Since f_0 is fixed to the value for 45°N, Eq. (1) yields a streamfunction tendency, which can be compared with the streamfunction-like height anomalies.

Trenberth (1981) shows that the power spectrum of v is dominated by high-frequency fluctuations. Unfiltered meridional wind velocity v is thus used to illustrate the spatial pattern and downstream propagation of the synoptic waves.

Following Nakamura and Wallace (1990), the daily anomalies of a given variable at each grid point are defined as its departure from the local value of the climatological-mean annual cycle. The annual cycle is obtained from the sum of the annual mean and first three harmonics of the 365-day climatological time series. The anomalous time series computed in this way contain both intraseasonal and interannual fluctuations.

The period of investigation consists of 62 winter seasons from 1948/1949 to 2009/1010 based on the NCEP–NCAR reanalysis and 1999 winter seasons based on the CM2.1 simulation. Winter is defined as the 121-day period starting from 1 December.

d. Identification of persistent events

Most of the previous studies examine eddy–mean flow interactions over the NP and NA basins separately (e.g., Wallace et al. 1988). However, as noted in LL12,

TABLE 1. Summary statistics for the two types of persistent events (FPI+ and FPI−) based on observations and the CM2.1 simulation. If the statistics for El Niño and La Niña winters (see second and third column of each grouping in the table) are significantly different at 95% confidence based on a standard Student's *t* test, the values are shown in bold type.

Type	Dataset	No. of events			No. of events per DJFM season			Avg. No. of days per DJFM season			Avg. duration (days)		
		All	EN	LN	All	EN	LN	All	EN	LN	All	EN	LN
FPI+	OBS	27	9	0	0.4	0.9	0.0	18.9	46.4	5.8	17.7	26.0	NA
	CM2.1	956	359	20	0.5	1.4	0.1	19.4	60.0	5.2	25.1	35.5	16.4
FPI−	OBS	31	0	13	0.5	0	1.4	19.4	1.3	41.3	20.5	NA	19.1
	CM2.1	1102	17	234	0.6	0.1	1.1	19.3	2.2	37.0	22.1	14.2	25.3

circulation anomalies appear to be more zonally symmetric during ENSO events. In addition, strong linkage between the Pacific and Atlantic storm tracks has been identified by James and Burkhardt (2006), thus arguing against the treatment of the two storm tracks as distinct, independent circulation systems. Therefore, to characterize the flow variability associated with ENSO events, a broad region encompassing both the NP and NA sectors (15° – 85° N, 160° E– 0° – 30° E) is considered in our study. A daily time series depicting the low-frequency variability of the flow pattern associated with ENSO events is obtained by computing the spatial correlation coefficients between the area-weighted daily low-pass-filtered Z_{250} anomalies and the seasonal Z_{250} composite map associated with the late winter El Niño events (see Fig. 8 in LL12). The gross features of various figures shown in the following sections are not sensitive to the exact spatial domain chosen for this data projection.

The daily value of the flow pattern index (FPI) as computed using the above procedure are normalized by the standard deviations of the entire time series. A $FPI \pm$ day is defined as any day in which the FPI exceeds ± 1.0 . A persistent $FPI \pm$ episode is considered to occur when the daily standardized FPI exceeds ± 1.0 for at least 10 consecutive days. Once a persistent episode is determined, the onset (decay) day is defined as the first (last) day of that episode. The duration criteria of 10 days has been used in previous studies (Dole and Gordon 1983; Higgins and Schubert 1996, 1997). We choose a threshold amplitude value of 1.0 so that the typical event is sufficiently strong, and that an adequate population of events is captured for statistical analysis. Following Nakamura and Wallace (1990) and Feldstein (1998), if the decay of a persistent anomaly is followed by the onset of another anomaly pattern with the same polarity within 10 days, these two periods are merged and treated as one episode. There is a total of 27 FPI+ and 31 FPI− episodes based on NCEP–NCAR reanalysis data for the 1948–2010 period and 956 FPI+ and 1102 FPI− episodes based on the 2000-yr CM2.1 simulation (see Table 1).

3. Relationships among FPI, ENSO, and NAO

a. Dependence of the persistent events on the phase of ENSO

In accord with the definition of FPI (see section 2d), the spatial patterns associated with FPI+ and FPI− days (not shown) bear similarities to those associated with El Niño and La Niña, respectively. This correspondence can be illustrated by showing the total number of FPI+ and FPI− days for each December–March (DJFM) season in warm and cold ENSO events.

Figure 1a shows the observed total number of FPI+ days (see red shaded columns) and FPI− days (blue columns) in each warm ENSO event. Analogous statistics for cold ENSO events are given in Fig. 1b. A warm (cold) ENSO is identified when the DJF-mean Niño-3 index (see definition in section 2b) is more than 0.5σ above (below) the time mean. A lower threshold of the Niño-3 amplitude is used here to include weak ENSO winters. In a majority of warm ENSO events, the number of FPI+ days is larger than the number of FPI− days. The number of FPI+ days in most of the warm ENSO winters is above the average number of FPI+ days for all winters in the 1948–2009 period (i.e., 18.9 days; see red solid line in Fig. 1a). In contrast, the number of FPI− days is below the average number of FPI− days (i.e., 19.3 days; see blue dashed line in Fig. 1a). The opposite situation holds in the cold ENSO events (see Fig. 1b).

The persistence characteristics of the $FPI \pm$ events can be illustrated by compositing the temporal evolution of 8-day low-pass-filtered FPI indices relative to the onset day, as shown for model data in Fig. 2. This procedure has been performed separately over the persistent episodes during El Niño winters only, La Niña winters only, and all winters. The simulated El Niño and La Niña winters are identical to those examined in LL12. For the persistent FPI+ events (Fig. 2a), the FPI index during El Niño winters (red curve) stays above 1σ longer than the FPI during La Niña winters (blue curve). The opposite situation holds in the persistent FPI− events (Fig. 2b). By applying a two-tailed Student's *t* test, it is found that the

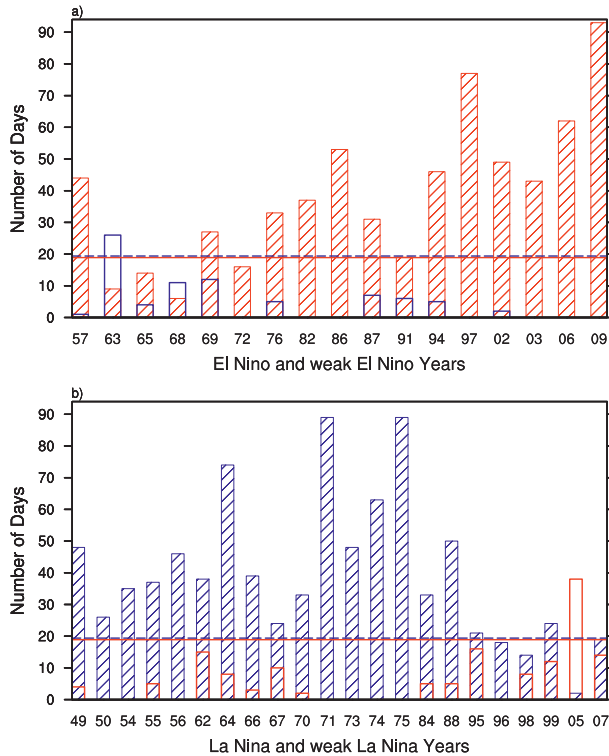


FIG. 1. Number of positive (red columns) and negative (blue columns) FPI days for each (a) El Niño and (b) La Niña winter season based on the NCEP–NCAR reanalysis. A positive (negative) FPI day is defined as any day in which FPI (index depicting spatial projection of 250-hPa geopotential height upon the flow pattern associated with ENSO; see text for more detail) exceeds $\pm 1.0\sigma$. An El Niño (La Niña) winter is identified when the DJF-mean Niño-3 index exceeds $\pm 0.5\sigma$. The average number of FPI+ and FPI- days for all winters are shown as the red solid and blue dashed lines, respectively, in each panel.

composite values of the FPI in El Niño and La Niña winters are statistically different at the 99% confidence level beyond 6 and 10 days for the persistent FPI+ and FPI- events, respectively.

The dependence of the characteristics of the persistent FPI events on the phase of ENSO is further delineated by computing the averaged number, frequency, and duration of the FPI \pm events, as well as averaged number of FPI \pm days separately for all winters, El Niño winters only, and La Niña winters only, based on both observations and model simulation. These statistics are displayed in Table 1. The average number of both FPI+ and FPI- days for all winters is approximately 20 for both observations and simulation (see also Fig. 1). The number of FPI+ days in El Niño winters is significantly larger than the all-winter average and is statistically significantly larger than the corresponding counts in La Niña winters by a factor of about 8 (12) for observations (model data). Moreover, the simulated average duration

of persistent FPI+ events in El Niño winters is almost twice as long as that in La Niña winters (see also Fig. 2a). Conversely, FPI- events are more frequent and longer lasting in La Niña events.

b. NAO phase during the persistent circulation anomalies

To examine the phase of the NAO during the persistent FPI \pm events, the average value and probability density functions (PDFs) of the normalized daily NAO index during persistent FPI \pm events are calculated and compared in this subsection. The daily NAO index is constructed by computing the spatial correlation coefficient between the area-weighted daily low-pass-filtered SLP field and the spatial pattern of the leading EOF of the SLP field over the NA region in the DJFM-mean winter season (similar to Fig. 5 of LL12, but for the DJFM-mean season).

The observed values of normalized daily NAO index, as computed based on the average over 478 (637) days within the duration of persistent FPI+ (FPI-) events, are -0.33 ($+0.13$). The difference between these composite values is statistically significant on the basis of a *t* test (*p* value < 0.01). Differences between composite values of the normalized NAO index based on FPI+ and FPI- events in the CM2.1 simulation are also found to be statistically significant (i.e., -0.63 versus $+0.60$, *p* value < 0.01).

The PDFs of the daily NAO index during the persistent FPI+ and FPI- events are compared for the NCEP–NCAR reanalysis (Fig. 3a) and CM2.1 simulation (Fig. 3b). Pronounced shifts in the distribution toward negative and positive NAO values are apparent for the simulated FPI+ and FPI- events, respectively. The PDFs for FPI+ and FPI- events are statistically different (*p* value < 0.01) using a Kolmogorov–Smirnov test (Smirnov 1948), for both NCEP and CM2.1 datasets.

It should be noted that the difference between both the composite value and PDFs of NAO indices for persistent FPI+ and FPI- are less distinct in observations than in the model simulation. This relatively weaker NAO response in observations is possibly due to the southwest (SW)-to-northeast (NE)-oriented wave packet over NA in the downstream eddy development, so that the barotropic forcing of the embedded synoptic eddies is also displaced northeastward relative to the model counterpart (see further discussion in sections 4 and 5).

4. Eddy-mean flow interactions during persistent FPI+ and FPI- events

We shall henceforth focus on the behavior of the synoptic-scale eddies and their interactions with the

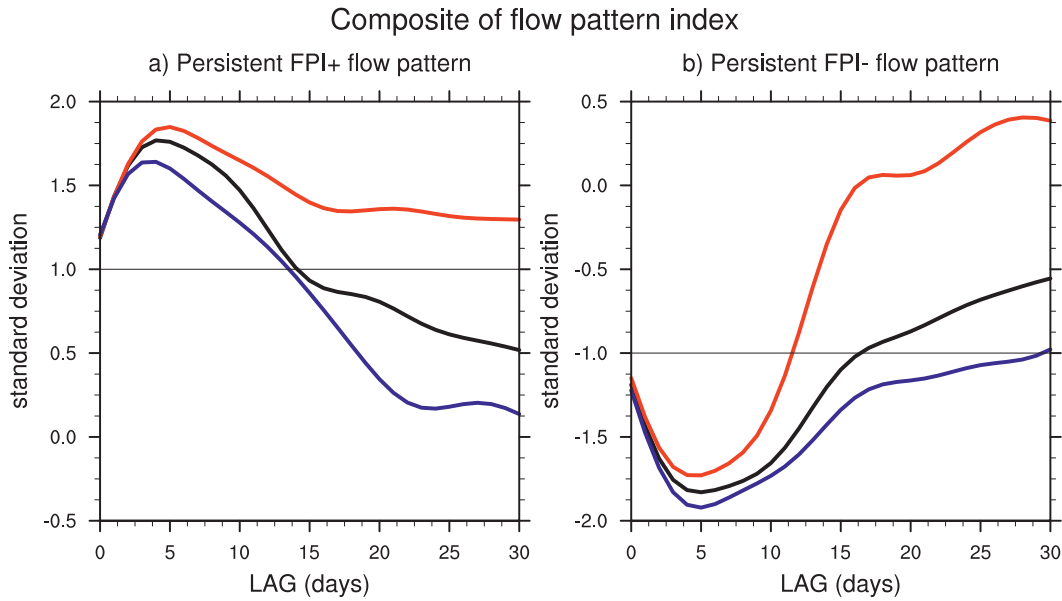


FIG. 2. Time series of the composites of the 8-day low-pass-filtered FPI based on the CM2.1 simulation. Composites are computed at various lags relative to the onset day of each persistent FPI event and are based on the persistent (left) FPI+ and (right) FPI- episodes during El Niño winters only (red curve), La Niña winters only (blue curve), and all winters (black curve).

background flow during the persistent FPI \pm events. For each persistent episode selected using the procedure in section 2d, simple time means are taken of the anomalous fields (see definition in section 2c) over the duration of that episode. Composites are then obtained by averaging over the means for all episodes.

a. Composites of persistent FPI+ events

Figure 4 shows the composites of 250-hPa low-pass-filtered geopotential height Z and envelope function Z_e (top panels), extended \mathbf{E} vectors and eddy-induced height tendency ($\partial Z/\partial t$, middle panels), and low-pass-filtered SLP

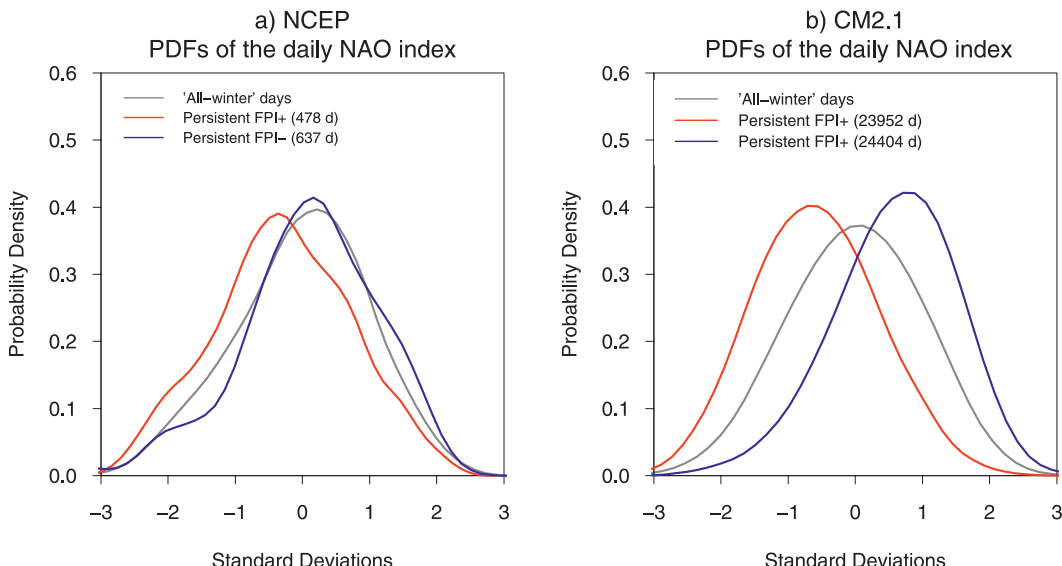


FIG. 3. PDFs of the normalized daily NAO indices for days within the persistent FPI+ events (red curve), persistent FPI- events (blue curve), and “all-winter” days (gray curve). Results based on the (left) NCEP–NCAR reanalysis and (right) CM2.1 simulation are shown.

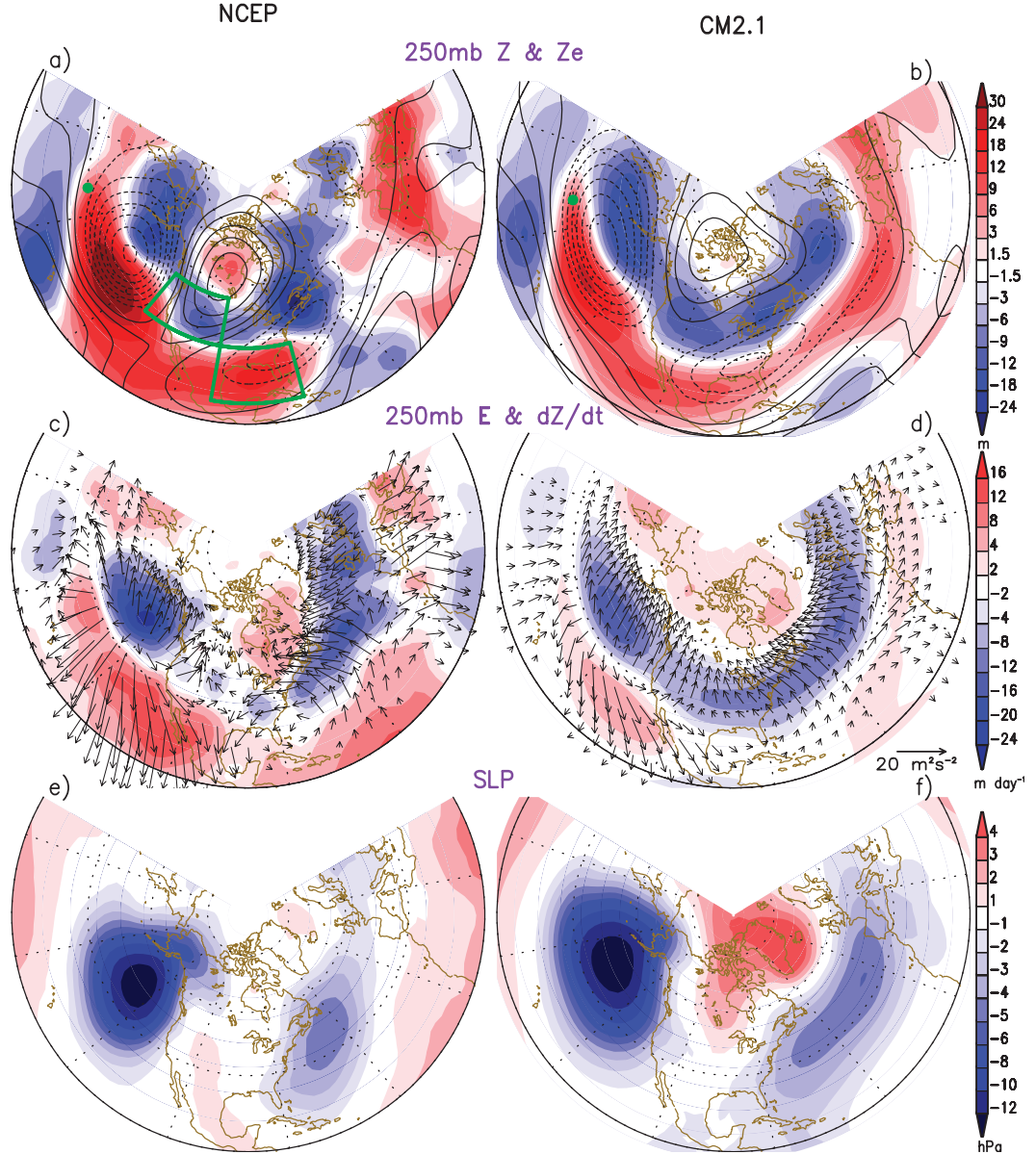


FIG. 4. Horizontal distribution of composites of the (a),(b) 8-day low-pass-filtered 250-hPa geopotential height (contours, interval: 30 m; dashed contours indicate negative values) and 250-hPa envelope function (shading, see scale bar at right), (c),(d) extended \mathbf{E} vectors (arrows, see scale bar at right) and eddy-induced height tendencies (shading, see scale bar at right), and (e),(f) 8-day low-pass-filtered sea level pressure (shading, see scale at right). The composites are averaged over the duration of all persistent FPI+ events. Results based on the (left) NCEP–NCAR reanalysis and (right) CM2.1 simulation are shown. The outermost latitude circle represents 15°N. The green dot in (a),(b) denotes the location of the reference point for the one-point lagged regression analysis in Fig. 6. The green boxes in (a) depict the boundaries of regions used for computing the SPI in section 5b.

(bottom panels) averaged over all selected FPI+ events. The observational and model results are shown in the left and right panels of Fig. 4, respectively. The observed composite pattern for 250-hPa low-frequency Z (contours in Fig. 4a) is characterized by a wave train (Wallace and Gutzler 1981) over the NP and North America sector. The anomalous height pattern over the NP sector is indicative

of a strengthened Pacific subtropical jet stream, which is in turn associated with enhanced eddy activity along the Pacific storm track near 35°N (see shading in Fig. 4a).

At the eastern end of the Pacific storm track, strong divergence of the \mathbf{E} vectors is discernible in both observations and simulation, with northward-directed arrows north of the storm track, and southeastward arrows

farther south. This configuration implies that the eddy momentum convergence leads to acceleration of the westerly mean flow (e.g., Trenberth 1986), reinforcement of the subtropical westerly anomalies at this location, as well as strengthening of storm track activities farther east over the southern United States/Gulf of Mexico. Farther downstream over the western and central Atlantic, the anomalous \mathbf{E} vectors are mostly divergent (leading to zonal flow acceleration) near 30°N and convergent (zonal flow deceleration) near 50°N . The cyclonic curvature of \mathbf{E} in midlatitude NA is indicative of northward wind acceleration (e.g., Trenberth 1986). The above configuration of zonal and meridional wind changes is consistent with negative height tendency $\partial Z/\partial t$ in the temperate zone of NA (see shading in Figs. 4c,d). This negative center is displaced eastward of the height anomaly (see contours in Figs. 4a,b) by 20° of longitude in observations and 40° in simulation. Such coherent eastward extension of negative height tendencies over the Atlantic sector has been emphasized in LL12.

At the surface, the observed pattern displays a low pressure anomaly over the central–western Atlantic near 35°N (Fig. 4e). This negative anomaly tilts northeastward over the eastern Atlantic. This feature is consistent with the northeastward displacement of the negative height tendency (see shading in Fig. 4c). In the CM2.1 simulation, the negative SLP anomaly in the subtropical NA is more zonally oriented and extends from the southeastern United States all the way across the Atlantic. This pattern is consistent with the zonal extension of the negative height tendencies over the Atlantic (see shading in Fig. 4d) and zonally oriented wave packet propagating across NA (see Figs. 6k,l to be presented later in this paper).

b. Composites of persistent FPI $-$ events

The polarity of the low-frequency anomalies in Z at 250 hPa and in SLP during observed persistent FPI $-$ events (Figs. 5a and 5e) is opposite to that for FPI $+$ events. The positive anomaly center to the south of Alaska is typical of the classic blocking situation over NP (e.g., Dole and Gordon 1983; Renwick and Wallace 1996). This blocking pattern is accompanied by notable diversions in the Pacific storm track and background westerlies. As indicated by Z_e (shading in Fig. 5a), the Pacific storm track is more active than its climatological mean to the north of the anomalous high and in the subtropics, whereas suppressed activity prevails in the zone situated between these two active sites. The relative quiescent belt along 35°N is characterized by strong convergence of the \mathbf{E} vectors (Fig. 5c), which implies zonal wind deceleration. Negative (positive) height anomalies over the northwestern (southeastern) quadrant of the North

America (contours in Fig. 5a) are indicative of strengthened southwesterly flow over much of the interior of this continent. The slightly enhanced eddy activity over eastern Canada together with the diminished activity over the southeastern U.S. (shading in Fig. 5a) is indicative of the northward shift of the Atlantic storm track.

The principal features of the simulated patterns in the right panels of Fig. 4 and Fig. 5 are in overall agreement with their observational counterparts. Of particular note are the more zonally extended and better organized signals of $\partial Z/\partial t$ over NA in the model patterns as compared to the observations. Generally speaking, observed inferences on eddy–mean flow interactions are also applicable to the much larger samples of persistent events generated by the CM2.1 simulation.

The strength and preferred location of $\partial Z/\partial t$ over NA, as shown in Figs. 4 and 5 for persistent episodes, bear some similarities to the corresponding charts shown for the ENSO composites of seasonal means (Figs. 8 and 9 in LL12). The comparability of these two sets of results indicate that eddy forcing during the persistent episodes plays an important role in determining the phase and amplitude of the seasonal averaged features. These findings also suggest that, during the persistent episodes, transient eddies can efficiently induce cyclonic or anti-cyclonic tendencies over NA.

5. Linkage between Pacific and Atlantic variability through downstream development

a. One-point lagged regression patterns based on persistent FPI $+$ events

Patterns showing the distributions of lagged correlation coefficients between the fluctuations at a fixed reference point and those at all other points in the analysis domain are often referred to as “one-point lag-correlation maps.” These charts have been widely used to study the horizontal structure and time variation of waves and wave packets (e.g., Blackmon et al. 1984a,b; Wallace et al. 1988). Since we are more interested in the relative amplitude of wave disturbances in different geographical regions, we shall devote our attention to the spatial patterns of lagged regression coefficients, following Lim and Wallace (1991) and Chang (1993). The lagged regression coefficient $b(\lambda, \phi, \tau)$ at a particular longitude λ and latitude ϕ at lag time τ is calculated as

$$b(\lambda, \phi, \tau) = \frac{\langle v'(\lambda_0, \phi_0, t)v'(\lambda, \phi, t + \tau) \rangle}{\sigma[v'(\lambda_0, \phi_0, t)]}, \quad (2)$$

where λ_0 and ϕ_0 are the longitude and latitude, respectively, for the time series at the reference grid point,

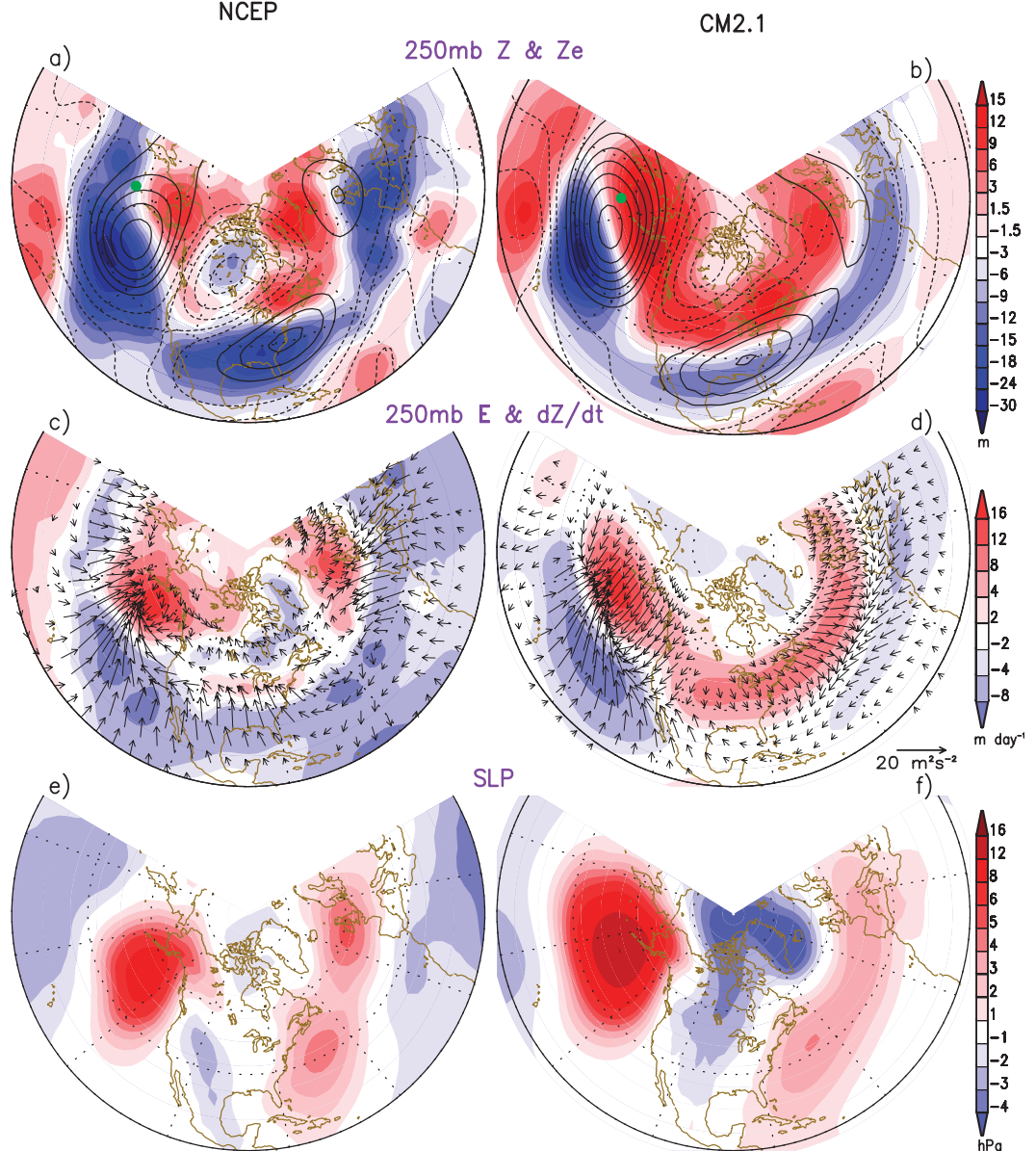


FIG. 5. As in Fig. 4, but for results based on persistent FPI–events. The green dot in (a),(b) denotes the location of the reference point for the one-point lagged regression analysis in Fig. 7.

$v'(\lambda, \phi, t)$ is the deviation of the unfiltered 250-hPa meridional velocity from its corresponding time mean at that grid point, $v'(\lambda, \phi, t) = v(\lambda, \phi, t) - \bar{v}(\lambda, \phi, t)$, $\sigma^2[v'(\lambda_0, \phi_0, t)] = \langle (v'(\lambda_0, \phi_0, t))^2 \rangle$, the overbar indicates a temporal average from the onset day to the decay day of individual persistent episode, the angle bracket denotes the ensemble average over all persistent episodes, and τ is the number of days by which the time series $v'(\lambda, \phi)$ lags the reference time series $v'(\lambda_0, \phi_0)$. The statistical significance of the regression coefficient is estimated by applying the Student's t test to the

corresponding correlation coefficient r , and assuming 1 degree of freedom per 10 days (which corresponds to the typical time scale of persistent events).

It should be pointed out that the above-mentioned previous studies using this one-point lagged correlation or regression technique are based on the average over “all-winter” days. However, because of the large meridional variation of the trajectories for both individual eddies and the entire wave packets, the signal of interest is often diluted in such climatological lagged correlation or regression maps. To highlight the features related to

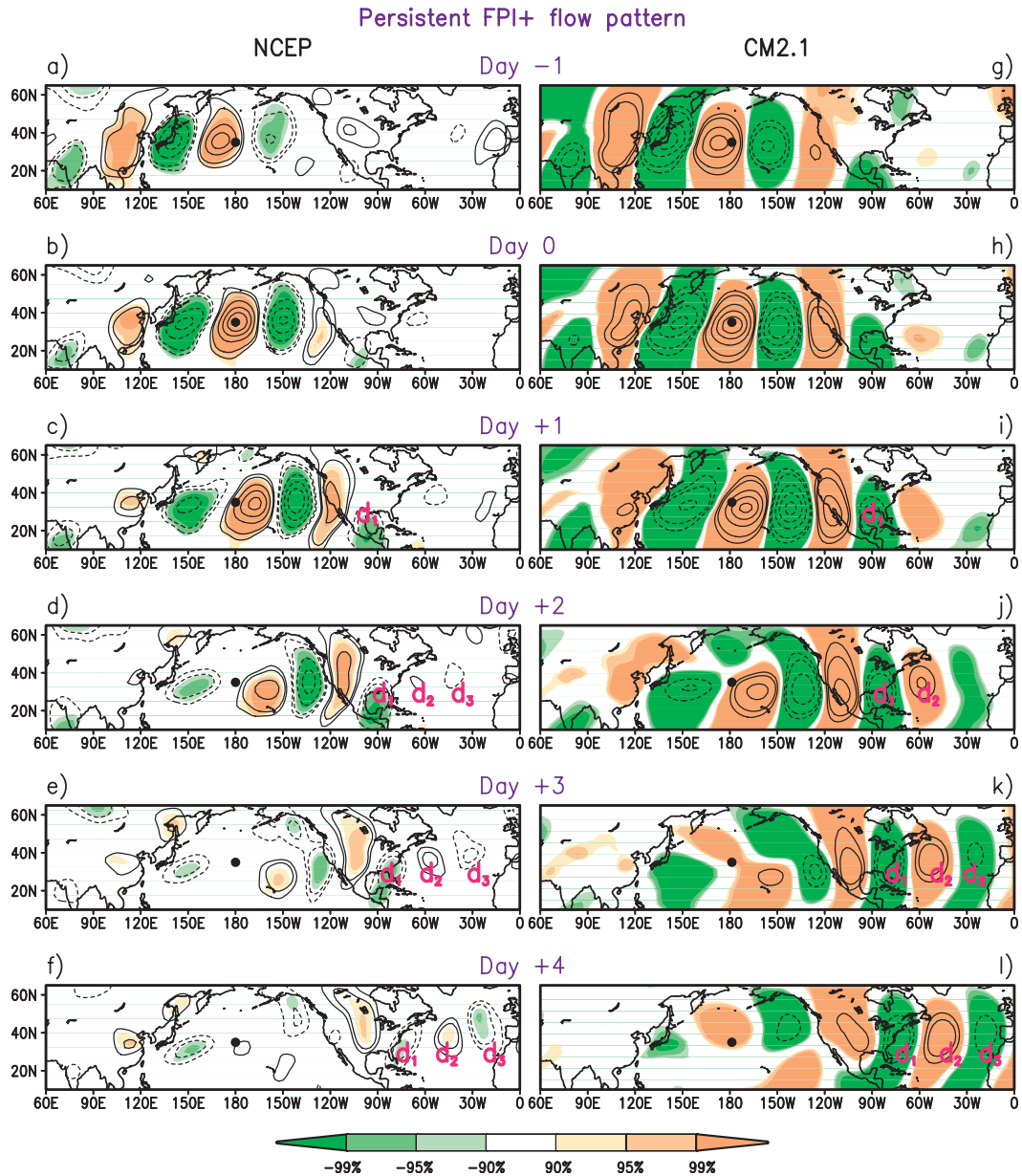


FIG. 6. One-point lagged regression maps of unfiltered 250-hPa meridional velocity v anomalies during the persistent FPI+ events. The reference time series is 250-hPa unfiltered v on day 0 at $(35^{\circ}\text{N}, 180^{\circ})$, as indicated by the black dot in each panel and the green dot in Figs. 4a,b. Maps for lags of $-1, 0, +1, +2, +3$, and $+4$ days are shown. Results based on the (left) NCEP–NCAR reanalysis and (right) CM2.1 simulation are shown. The regression coefficients are contoured at $\pm 2, \pm 3, \pm 6, \pm 9$, and $\pm 12 \text{ m s}^{-1}$. Dashed contours indicate negative values. Shading indicates signals exceeding 90%, 95%, and 99% confidence levels based on Student's t test (see scale at bottom).

eddy development, we limit the sample populations to those episodes with persistent flow pattern or storm-path pattern (see section 5b). A similar approach has been taken by Hakim (2003), who uses ensemble averaging of cases that share common ray paths as an indication of wave packet evolution and concludes that Pacific wave packets often serve as “seeding” for the Atlantic storm track.

Left panels of Fig. 6 show the one-point lag-regression maps of unfiltered 250-hPa meridional velocity anomalies for lags of $-1, 0, +1, +2, +3$, and $+4$ days, as computed using observational data. The reference point is located at $(35^{\circ}\text{N}, 180^{\circ})$, that is, along the axis of the Pacific storm track (see green dot in Fig. 4a). On day 0 (Fig. 6b), the zonally oriented wave train extends from East Asia all the way across the Pacific. The consecutive

positive and negative centers are separated approximately 30° longitude, thus implying a wavelength of about 6000 km. As estimated from the time-lagged regressions from day -1 to day $+3$, the individual centers travel eastward by about 40° in 4 days, thus yielding a phase speed of about 13 m s^{-1} and a period of about 6 days.

Comparison between the regression pattern on day -1 and that on day $+1$ reveals that relatively higher wave amplitudes are observed on the upstream side of the reference center on day -1 and on the downstream side on day $+1$. These asymmetries of the regression patterns with respect to the reference point and to the time lag clearly indicate the evolution of an eastward-propagating wave packet, with successive growth (decay) of troughs and ridges downstream (upstream) of the reference site. On day $+1$, the leading edge of the packet, labeled with “ d_1 ” in Fig. 6c, appears over the southern portion of the North America continent. This center experiences substantial growth on day $+2$ and two new centers (“ d_2 ” and “ d_3 ”) are seen to emerge still farther downstream (Fig. 6d). The wave packet over NA preserves its coherence on days $+3$ and $+4$ (Figs. 6e,f), and the wave disturbances over NA are statistically significant on day $+4$.

The right panels of Fig. 6 show the corresponding patterns obtained from the CM2.1 simulation. The simulated results are in general agreement with the observational results with regards to the wavelength and period. The coherent wave packet over NA is most evident on days $+3$ and days $+4$ (Figs. 6k,l). It should also be noted that the wave packet over NA is aligned more zonally in simulation than that in observations. The southwest-to-northeast-oriented wave packet in observations may be related to the northeastward-displaced transient eddy forcing (see shading in Fig. 4c) and the negative SLP anomaly over the midlatitude NA (Fig. 4e).

We have also examined similar one-point lagged-regression maps but based on the average over all-winter days for both the NCEP–NCAR reanalysis dataset and CM2.1 simulation (not shown). The coherent wave packet propagation across NA is not apparent in the lagged regression patterns based on both datasets. These findings compare well with previous observational results (Chang 1993, see his Fig. 5; Chang and Yu 1999, see their Fig. 2), and illustrate that the successive eddy downstream development from NP to the NA is particularly strong during the persistent FPI+ episodes.

Figure 7 shows the observed and simulated lagged-regression maps based on the persistent FPI– events. The reference point is located farther north (e.g., 50°N , 180°) in view of the northward shift of Pacific storm track activity during these persistent FPI– events (see Figs. 5a,b).

Since the Pacific wave packet originates from a higher latitude, it refracts equatorward with a dominant southwest–northeast tilt (e.g., James 1994; Orlanski 2003) as it approaches the west coast of North America on day $+2$ (Figs. 7d,j). This characteristic indicates northward eddy momentum flux and is consistent with the northward shift of the jet and associated storm-track activity. On days $+3$ and $+4$, the signal over NA is discernible in observations. Although the amplitude of the simulated disturbances over NA is weak, these signals are statistically significant in the model patterns (Figs. 7k,l). The lagged-regression analysis for FPI– events is also repeated using the reference point at (35°N , 180°), and no discernible signal is found over NA (results not shown). The findings in Fig. 7 indicate the existence of the downstream development of wave packet from the northern route during the persistent FPI– events, although the signal is weaker than that associated with the southern route during the persistent FPI+ events.

b. One-point lagged-regression patterns based on persistent storm-track events

The interannual variations of the latitudinal position of the zone of maximum transient eddy activities over North America, and their relationship to both ENSO and NAO has been illustrated in LL12. However, it is not feasible to infer from seasonal statistics presented in LL12 the behavior of individual eddies as they propagate from NP to NA. The recent study of Seager et al. (2010b) shows that the transient waves propagate along a more southern path toward southwestern North America during El Niño and a more northern route toward the Pacific Northwest during La Niña. However, these authors do not investigate the propagation of those waves farther eastward to the NA sector. We have highlighted these two preferred paths of eddy propagation during the persistent FPI+ and FPI– events in Figs. 4a,b and Figs. 5a,b. It is hence of interest to study the downstream eddy development from NP toward NA during those periods of persistent eddy activity along these two preferred paths. In view of the important role of storm-track activities over southern United States/Gulf of Mexico and northwestern North America in linking the circulation anomalies over NP and NA, a daily storm path index (SPI) is defined by taking the normalized difference between Z_e averaged over these two regions (i.e., 20° – 35°N , 100° – 70°W and 35° – 50°N , 130° – 100°W ; see boxed areas in Fig. 4a). Persistent SPI \pm events are selected using the same methodology as described in section 2d (using amplitude and duration thresholds of $\pm 1\sigma$ and 10 days, respectively). This procedure yields 13 SPI+ and 19 SPI– cases based on the 62-yr NCEP–NCAR reanalysis data, and 509 SPI+ and 487 SPI– cases based

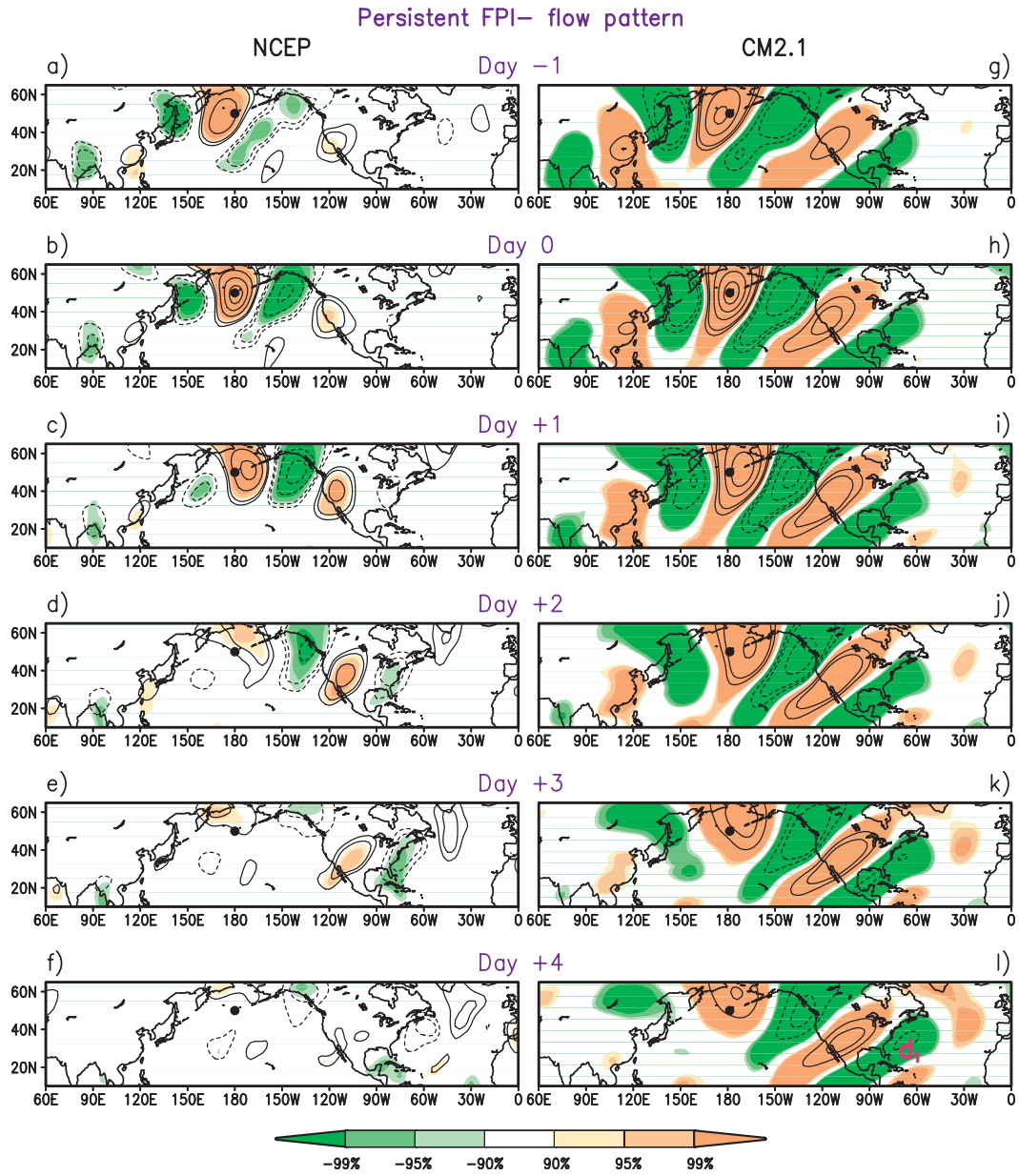


FIG. 7. As in Fig. 6, but for results based on persistent FPI $-$ events with reference point located at (50°N, 180°).

on the 2000-yr CM2.1 simulation. In analogy with the statistics for FPI $+$ ($-$) events (see Table 1), more frequent and long-lived SPI $+$ ($-$) episodes are observed and simulated during El Niño (La Niña) winters.

Using the same reference points as in Figs. 6 and 7, a one-point lagged-regression analysis is carried out over the duration of persistent SPI $+$ and SPI $-$ events, respectively. Since the number of observational cases is too small to generate statistically significant patterns, only the model results are shown in Fig. 8 for SPI $+$ (left panels) and SPI $-$ (right panels) events. During the

persistent SPI $+$ events, a coherent wave packet is evident and extends all the way to the eastern Atlantic on days +2 and +3. The evolution of the leading edge of the packet during the persistent SPI $+$ events bears a strong resemblance to that in the persistent FPI $+$ events, although the amplitudes of the disturbances on the leading edge of the packet based on the SPI $+$ events are almost twice as large as those for the FPI $+$ events (e.g., compare “ d_3 ” in Figs. 6k,l and Figs. 8e,f).

The downstream development of the wave packet from the northern route during the persistent SPI $-$ events

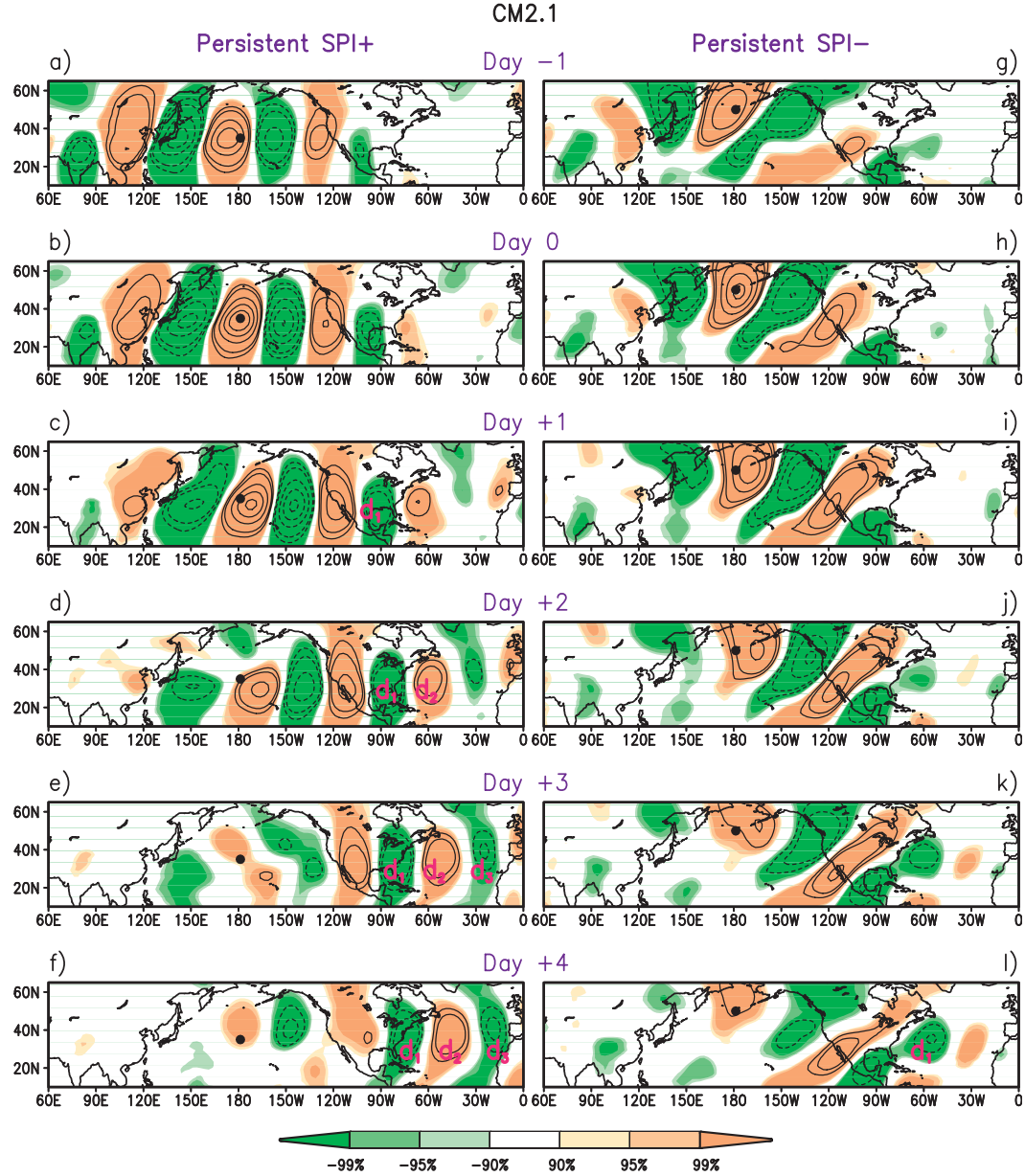


FIG. 8. As in Figs. 6 and 7, but for the persistent (left) SPI+ (see definition of SPI in the text) and (right) SPI- episodes based on the CM2.1 simulation.

(right panel of Fig. 8) is less evident than that from the southern route during the persistent SPI+ events. The amplitude of the disturbances is relatively weaker possibly because of the equatorward refraction as in the persistent FPI- events (see also Fig. 7). However, the disturbances over the NA on days +3 and +4 are still significant. Again, the amplitude of the disturbances on the leading edge of the packet based on the SPI- is also twice as large as that for the FPI- events (e.g., compare “ d_1 ” in Fig. 7l and Fig. 8l).

The strong packet evolution during the persistent SPI+ events indicates the importance of the persistent transient eddy activities over southern United States/Gulf of Mexico in the downstream development of the wave packet over NA. During the SPI+ episodes, the strong and steady eddy forcing of the synoptic eddies contributes to the formation of the negative phase of NAO. Since El Niño-related tropical forcing could enhance transient eddy activity over southern United States/Gulf of Mexico (see Fig. 8 in LL12), the results presented

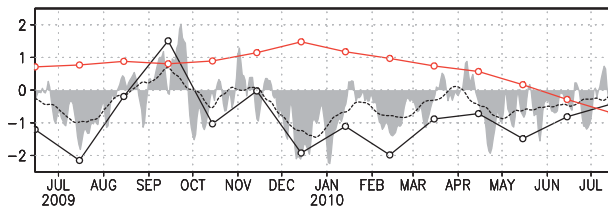


FIG. 9. The time series of daily NAO index (shading), 30-day running mean NAO index (dashed line), monthly mean NAO index (solid black line), and monthly ENSO index of Niño-3 (red line) for the 2009/10 winter. (The daily and monthly NAO indices are obtained online from <ftp://ftp.cpc.ncep.noaa.gov/cwlinks/norm.daily.nao.index.b500101.current.ascii>, and <http://www.cpc.ncep.noaa.gov/products/precip/CWlink/pna/norm.nao.monthly.b5001.current.ascii>, respectively.)

in this section hence provide additional evidence in support of the ENSO impact on the downstream development of the wave packets from the Pacific toward the eastern Atlantic.

A possible contributor to the strong downstream eddy development during the persistent SPI+ events could be the enhanced eddy kinetic energy over southern United States/Gulf of Mexico, since large positive anomalous Z_e are seen in this region during those episodes (see Figs. 4a,b).

6. Case study of the 2009/10 season

The 2009/10 winter season is characterized by a series of severe winter storms across the United States and Europe, which resulted in anomalously heavy seasonal snowfall over the central and eastern United States and northwestern Europe (Seager et al. 2010a). This season also coincides with a moderate El Niño and a persistent negative phase of the NAO. As shown in Fig. 9, the NAO index is mostly negative from December through March. The combination of El Niño and a negative NAO accentuates the atmospheric anomalies associated with these individual phenomena. In particular, the geopotential height anomaly exhibits a strong zonal symmetric pattern, with out-of-phase variations between anomalies at 40°N and those in the Arctic zone (see Fig. 13a in LL12 for ENSO+/NAO– winters; Fig. 1a in Cattiaux et al. 2010 for 2009/10 winter season). The storm track is shifted southward in both Pacific and Atlantic basins (see Fig. 13a in LL12). This strengthened linkage between the Pacific and Atlantic storm tracks is indicative of the propagation of transient disturbances all the way from NP to NA, with enhanced cyclone development over the United States. There are 70 ENSO+/NAO– winters in the 2000-yr span of the CM2.1 simulation, which suggests the return period of a joint occurrence of ENSO+ and NAO– (with both indices exceeding the 1σ threshold) is about 29 years.

Figure 10a shows the longitude–time distribution of 250-hPa unfiltered anomalous v for the December 2009–March 2010 period based on the NCEP–NCAR reanalysis data. Averages are taken over the 30°–45°N band. In most normal winters, the climatological ridge near 140°W tends to “block” the propagation of the eddies to the east (Orlanski 1998). However, the ridge in the 2009/10 winter (not shown) is much weaker than normal, so that many wave packets in the Pacific storm track can propagate across the continental United States toward NA. Chang (1993) and Chang et al. (2002) have similarly documented the coherent propagation of the wave packets for the 1983/84 and 1980/81 winters, respectively.

To delineate the relationships between the upper level circulation and developments near the surface, cyclone trajectories are superimposed in Fig. 10a using black dots. These paths of surface weather disturbances are obtained by tracking the center of maximum 1000-hPa geostrophic relative vorticity, ζ_g , on a $2.5^\circ \times 2.5^\circ$ latitude–longitude grid every 6 h during the lifetime of each identified winter storm. There is a total of 12 winter storms shown in Fig. 10a. The onset and decay dates of these episodes are obtained from http://www.hpc.ncep.noaa.gov/winter_storm_summaries/winter_storm_summaries.shtml. Tracking the minima in SLP yields similar trajectories. The abscissa and ordinate of each black dot correspond to the longitude and date of the occurrence of the ζ_g maxima, respectively. As seen in Fig. 10a, almost all surface cyclones are collocated with positive wind anomalies at 250 hPa. This relationship indicates that the upper-level low/trough is typically situated to the west of the surface low/trough. Since upper-level divergence and lower-level convergence prevail in the air column downwind of the upper-level trough (e.g., Holton 2004), this vertical structure provides a favorable environment for cyclogenesis (Petterssen and Smebye 1971).

The daily evolution in the amplitude of the envelope function Z_e at 250 hPa in this winter is shown in the time–longitude diagram in Fig. 10b. The latitude of the storm-track axis is determined for each calendar day by tracking the peak value of Z_e value along each meridian. Values of Z_e are averaged over a 10° -latitude interval centered on the storm-track axis on each meridian. This procedure hence takes into account the meridional displacement of the storm-track axis. In Fig. 10b, we can identify several cases with the band of large Z_e extending across the Pacific and North America into the Atlantic. These signals are indicative of the downstream development of the wave packet during persistent SPI+ events as suggested in section 5b.

We proceed to examine the role of eddy vorticity forcing in the evolution of the circulation over NA during the 2009/10 winter. The time–latitude sections of the following

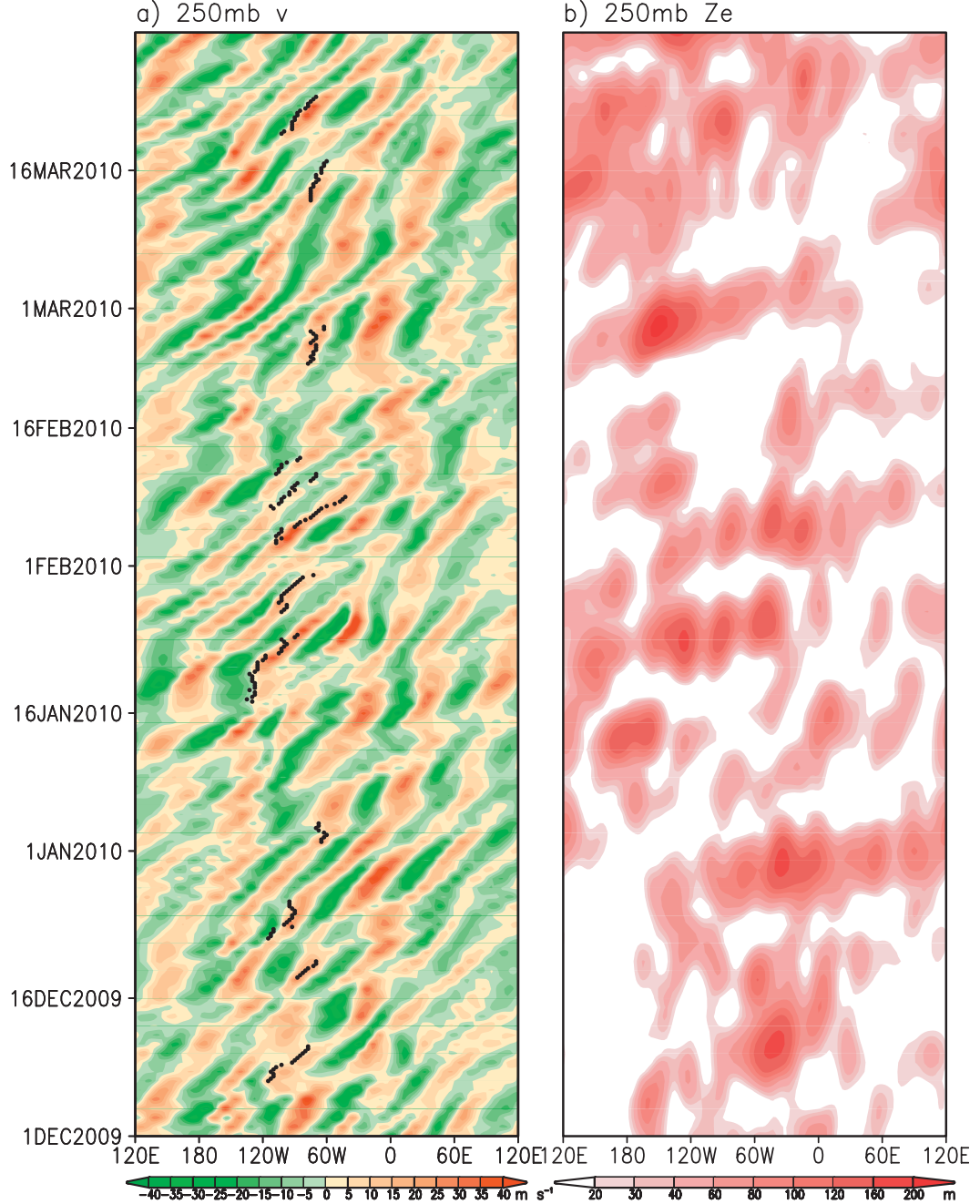


FIG. 10. Longitude-time (Hovmöller) sections of (a) 250-hPa unfiltered anomalous v averaged over 30° – 45° N and (b) 250-hPa anomalous envelope function (Z_e). The amplitude in (b) at each meridian is obtained by averaging over a 10° latitude interval centered on the storm-track axis in Z_e and then applying Gaussian spatial smoothing with width of 60° (one wavelength) along the longitude axis. Each black dot in (a) denotes the time and longitude position of occurrence of the maxima of the 1000-hPa geostrophic relative vorticity every 6 h during the lifetime of each winter storm. Information on the identified winter storms is obtained from http://www.hpc.ncep.noaa.gov/winter_storm_summaries/winter_storm_summaries.shtml. See text for more details.

quantities are shown in Fig. 11: 250-hPa low-pass-filtered geopotential height anomalies Z (contours) and the envelope function Z_e (shading) in the upper panel, and 250-hPa Z (contours) and eddy-induced height

tendencies $\partial Z / \partial t$ (shading) in the lower panel. All values are based on longitudinal averages over the NA sector (i.e., 70° – 20° W). The strong negative Z anomalies at 40° N and positive anomalies near 65° N (contours in Fig. 11a)

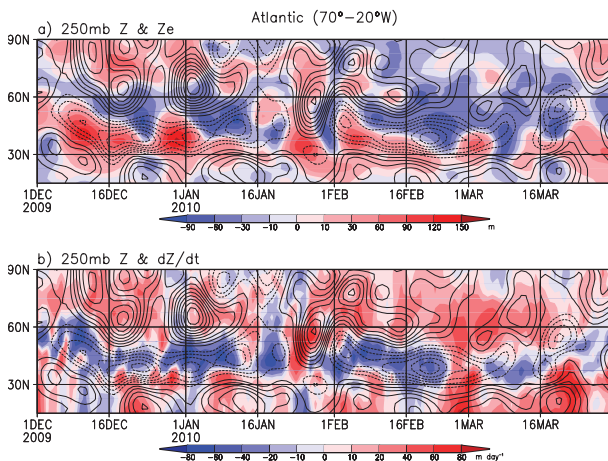


FIG. 11. Latitude-time sections of anomalous 250-hPa (a) 8-day low-pass-filtered Z (contours, interval: 50 m; dashed contours indicate negative values) and envelope function Z_e (shading, see scale bar at bottom) and (b) 8-day low-pass filtered Z (contours) and eddy-induced height tendency (shading, see scale bar at bottom). All data are averaged over the 70° – 20° W zone.

depict the prominent negative NAO phase in this winter season. The negative Z anomalies in middle latitudes are accompanied by strengthened eastward flows on their southern flank and weakened eastward flows on their northern flank. Such zonal wind variations in turn modulate the intensity of transient disturbances (as inferred from the pattern of Z_e), with positive and negative anomalies of Z_e occurring to the south and north of the midlatitude Z anomalies, respectively. The changes in the eddy-induced height tendencies ($\partial Z / \partial t$) are in phase with the local Z anomalies (Fig. 11b). This result confirms the strong feedbacks of eddy forcing on the ambient background flow in this particular winter.

7. Summary and discussion

The study of LL12 is extended to examine the role of transient eddies in the ENSO–NAO relationship during submonthly anomalous episodes. Our results indicate that ENSO events exert a strong influence on the frequency and duration of such episodes. Specifically, El Niño winters tend to favor persistent episodes with strengthened Pacific subtropical jet stream, equatorward-shifted Pacific storm track, enhanced cyclone activities along the Gulf of Mexico/southeastern United States, and a negative phase of the NAO. La Niña winters are accompanied by more frequent occurrence of poleward-shifted jet stream and storm track over the Pacific and a positive NAO phase.

Lagged regression analysis reveals strong downstream development of wave packets during the observed and

simulated FPI+ episodes. The leading edge of the packet travels from North America to the western Atlantic in 1–2 days. In such development, synoptic-scale transient eddies induce negative $\partial Z / \partial t$ over the region corresponding to the southern lobe of the NAO. The more frequent occurrence and longer duration of those episodes during El Niño winters are accompanied by stronger and more steady transient eddy forcings, as well as farther eastward penetration of the wave packets to the NA sector. These effects contribute to the higher incidence of negative NAO-like anomalies in El Niño winters. These results, as inferred from weather episodes with submonthly time scales, offer a more detailed perspective of eddy processes responsible for the ENSO–NAO relationships examined in LL12 using seasonal averages.

There are two possible explanations for the downstream extension of wave packets along the southern route across southern United States/Gulf of Mexico associated with El Niño winters. First, stronger eastward phase propagation of baroclinic eddies and eastward propagation of the entire wave packets are facilitated by the strengthened Pacific subtropical jet stream during the persistent FPI+ episodes. Second, the positive anomalies of Z_e near the Gulf of Mexico may contribute to increased eddy kinetic energy in this region during persistent SPI+ episodes (see Figs. 4a,b). Since these two conditions often occur simultaneously, they may together contribute to the enhanced downstream extension of the wave packets.

It should also be pointed out that the downstream development of wave packets from the northern route through northwestern North America is less evident than that from the southern route. This is probably due to the equatorward refraction of the midlatitude waves with a dominant southwest-northeast tilt (e.g., James 1994; Orlanski 2003).

Most of the findings based on multiyear datasets are confirmed by a case study of the 2009/10 winter season, in which a strong negative NAO phase coincides with a moderate El Niño. It is shown that a majority of the severe winter storms over the United States in that season are associated with coherent upper level wave packets originating from NP and propagating across North America. Within this winter, there are many synoptic episodes in which a surface cyclone develops to the east of an upper-level trough embedded in a wave packet. These results indicate that surface cyclone development often occurs at the approach of an upper-level trough at the leading edge of the wave packet.

A number of studies consider the NAO as the remnant of upstream wave breaking (e.g., Benedict et al. 2004; Franzke et al. 2004; Riviére and Orlanski 2007; Strong

and Magnusdottir 2008a,b). These studies point out that anticyclonic and cyclonic wave breaking of the synoptic eddies could lead to the formation of the positive and negative phase of the NAO, respectively. In particular, Rivière and Orlanski (2007) note that the anticyclonic and cyclonic breaking over NA of synoptic-scale waves originating from the eastern Pacific is crucial for determining the NAO phase. Anticyclonic and cyclonic wave breaking, as in the LC1 and LC2 idealized baroclinic wave life cycles (e.g., see Thorncroft et al. 1993), is characterized by northeast (NE)–southwest (SW) and southeast (SE)–northwest (NW) tilt of the trough/ridge axes, respectively. In this study, the SE–NW (NE–SW) orientations of the synoptic-scale eddies near the eastern Pacific during the persistent SPI+ (SPI−) (Fig. 8) episodes also support the above notion that the phase of the NAO is influenced by the transient waves originating from the eastern Pacific.

Acknowledgments. We are indebted to Isidoro Orlanski, Rym Msadek, and Dave Thompson for providing comments and suggestions, and to Martin Hoerling for helpful discussions. This report was prepared by YL under Award NA17RJ2612 and NA08OAR4320752 from the National Oceanic and Atmospheric Administration, U.S. Department of Commerce. The statements, findings, conclusions, and recommendations are those of the author(s) and do not necessarily reflect the views of the National Oceanic and Atmospheric Administration or the U.S. Department of Commerce.

REFERENCES

- Benedict, J. J., S. Lee, and S. B. Feldstein, 2004: Synoptic view of the North Atlantic Oscillation. *J. Atmos. Sci.*, **61**, 121–144.
- Bjerknes, J., 1969: Atmospheric teleconnections from the equatorial Pacific. *Mon. Wea. Rev.*, **97**, 163–172.
- Blackmon, M. L., Y.-H. Lee, and J. M. Wallace, 1984a: Horizontal structure of 500-mb height fluctuations with long, intermediate, and short time scales. *J. Atmos. Sci.*, **41**, 961–979.
- , —, —, and H.-H. Hsu, 1984b: Time variation of 500-mb height fluctuations with long, intermediate, and short time scales as deduced from lag-correlation statistics. *J. Atmos. Sci.*, **41**, 981–991.
- Brönnimann, S., J. Luterbacher, J. Staehelin, T. M. Svendby, G. Hansen, and T. Svenne, 2004: Extreme climate of the global troposphere and stratosphere 1940–1942 related to El Niño. *Nature*, **431**, 971–974.
- , E. Xoplaki, C. Casty, A. Pauling, and J. Luterbacher, 2007: ENSO influence on Europe during the last centuries. *Climate Dyn.*, **28**, 181–197.
- Cattiaux, J., R. Vautard, C. Cassou, P. Yiou, V. Masson-Delmotte, and F. Codron, 2010: Winter 2010 in Europe: A cold extreme in a warming climate. *Geophys. Res. Lett.*, **37**, L20704, doi: 10.1029/2010GL044613.
- Chang, E. K. M., 1993: Downstream development of baroclinic waves as inferred from regression analysis. *J. Atmos. Sci.*, **50**, 2038–2053.
- , 1998: Poleward-propagating angular momentum perturbations induced by zonally symmetric heat sources in the tropics. *J. Atmos. Sci.*, **55**, 2229–2248.
- , 1999: Characteristics of wave packets in the upper troposphere. Part II: Seasonal and hemispheric variation. *J. Atmos. Sci.*, **56**, 1729–1747.
- , and D. B. Yu, 1999: Characteristics of wave packets in the upper troposphere. Part I: Northern Hemisphere winter. *J. Atmos. Sci.*, **56**, 1708–1728.
- , S. Lee, and K. L. Swanson, 2002: Storm-track dynamics. *J. Climate*, **15**, 2163–2183.
- Delworth, T. L., and Coauthors, 2006: GFDL's CM2 global coupled climate models. Part I: Formulation and simulation characteristics. *J. Climate*, **19**, 643–674.
- Dole, R. M., 1986: Persistent anomalies of the extratropical Northern Hemisphere wintertime circulation: Structure. *Mon. Wea. Rev.*, **114**, 178–207.
- , and N. D. Gordon, 1983: Persistent anomalies of the extratropical Northern Hemisphere wintertime circulation: Geographical distribution and regional persistence characteristics. *Mon. Wea. Rev.*, **111**, 1567–1586.
- Dong, B.-W., R. T. Sutton, S. P. Jewson, A. O'Neil, and J. M. Slingo, 2000: Predictable winter climate in the North Atlantic sector during the 1997–99 ENSO cycle. *Geophys. Res. Lett.*, **27**, 985–988.
- Duchon, C., 1979: Lanczos filtering in one and two dimensions. *J. Appl. Meteor.*, **18**, 1016–1022.
- Feldstein, S. B., 1998: The growth and decay of low-frequency anomalies in a GCM. *J. Atmos. Sci.*, **55**, 415–428.
- , 2000: The timescale, power spectra, and climate noise properties of teleconnection patterns. *J. Climate*, **13**, 4430–4440.
- Fraedrich, K., and K. Müller, 1992: Climate anomalies in Europe associated with ENSO extremes. *Int. J. Climatol.*, **12**, 25–31.
- Franzke, C., S. Lee, and S. B. Feldstein, 2004: Is the North Atlantic Oscillation a breaking wave? *J. Atmos. Sci.*, **61**, 145–160.
- Gnanadesikan, A., and Coauthors, 2006: GFDL's CM2 global coupled climate models. Part II: The baseline ocean simulation. *J. Climate*, **19**, 675–697.
- Griffies, S. M., M. J. Harrison, R. C. Pacanowski, and A. Rosati, 2004: A technical guide to MOM4. NOAA/Geophysical Fluid Dynamics Laboratory Ocean Group Tech. Rep. 5, 342 pp.
- Hakim, G. J., 2003: Developing wave packets in the North Pacific storm track. *Mon. Wea. Rev.*, **131**, 2824–2837.
- Higgins, R. W., and S. D. Schubert, 1996: Simulations of persistent North Pacific circulation anomalies and interhemispheric teleconnections. *J. Atmos. Sci.*, **53**, 188–207.
- , and —, 1997: Persistent North Pacific circulation anomalies and the tropical intraseasonal oscillation. *J. Climate*, **10**, 223–244.
- Hoerling, M. P., and M. Ting, 1994: Organization of extratropical transients during El Niño. *J. Climate*, **7**, 745–766.
- Holton, J. R., 2004: *An Introduction to Dynamic Meteorology*. 4th ed. Academic Press, 535 pp.
- Horel, J. D., and J. M. Wallace, 1981: Planetary-scale atmospheric phenomena associated with the Southern Oscillation. *Mon. Wea. Rev.*, **103**, 813–829.
- Ineson, S., and A. A. Scaife, 2009: The role of the stratosphere in the European climate response to El Niño. *Nat. Geosci.*, **2**, 32–36, doi:10.1038/ngeo381.

- James, I., 1994: *Introduction to Circulating Atmospheres*. Cambridge University Press, 422 pp.
- , and U. Burkhardt, 2006: A sidelong look at storm tracks. *Atmos. Sci. Lett.*, **7**, 69–74, doi:10.1002/asl.134.
- Kalnay, E., and Coauthors, 1996: The NCEP/NCAR 40-Year Reanalysis Project. *Bull. Amer. Meteor. Soc.*, **77**, 437–471.
- Lau, N.-C., A. Leetmaa, M. J. Nath, and H.-L. Wang, 2005: Influences of ENSO-induced Indo-Western Pacific SST anomalies on extratropical atmospheric variability during the boreal summer. *J. Climate*, **18**, 2922–2942.
- Li, Y., and N.-C. Lau, 2012: Impact of ENSO on the atmospheric variability over the North Atlantic in late winter—Role of transient eddies. *J. Climate*, **25**, 320–342.
- Lim, G. H., and J. M. Wallace, 1991: Structure and evolution of baroclinic waves as inferred from regression analysis. *J. Atmos. Sci.*, **48**, 1718–1732.
- Mathieu, P.-P., R. T. Sutton, B. Dong, and M. Collins, 2004: Predictability of winter climate over the North Atlantic/European region during ENSO events. *J. Climate*, **17**, 1953–1974.
- Merkel, U., and M. Latif, 2002: A high-resolution AGCM study of the El Niño impact on the North Atlantic/European sector. *Geophys. Res. Lett.*, **29**, 1291, doi:10.1029/2001GL013726.
- Moron, V., and I. Gouirand, 2003: Seasonal modulation of the El Niño–Southern Oscillation relationship with sea level pressure anomalies over the North Atlantic in October–March (1873–1996). *Int. J. Climatol.*, **37**, 143–155.
- Nakamura, H., and J. M. Wallace, 1990: Observed changes in baroclinic wave activity during the life cycles of low-frequency circulation anomalies. *J. Atmos. Sci.*, **47**, 1100–1116.
- , and A. Shimpo, 2004: Seasonal variations in the Southern Hemisphere storm tracks and jet streams as revealed in a reanalysis dataset. *J. Climate*, **17**, 1828–1844.
- , M. Nakamura, and J. L. Anderson, 1997: The role of high- and low-frequency dynamics in blocking formation. *Mon. Wea. Rev.*, **125**, 2074–2093.
- , T. Izumi, and T. Sampe, 2002: Interannual and decadal modulations recently observed in the Pacific storm track activity and East Asian winter monsoon. *J. Climate*, **15**, 1855–1874.
- Nigam, S., 2003: Teleconnections. *Encyclopedia of Atmospheric Sciences*, Vol. 6, J. R. Holton, J. A. Pyle, and J. A. Curry, Eds., Academic Press, 2243–2269.
- Orlanski, I., 1998: Poleward deflection of storm tracks. *J. Atmos. Sci.*, **55**, 2577–2602.
- , 2003: Bifurcation in eddy life cycles: Implications for storm-track variability. *J. Atmos. Sci.*, **60**, 993–1023.
- , 2005: A new look at the Pacific storm track variability: Sensitivity to tropical SSTs and to upstream seeding. *J. Atmos. Sci.*, **62**, 1367–1390.
- Petterssen, S., and S. J. Smebye, 1971: On the development of extratropical cyclones. *Quart. J. Roy. Meteor. Soc.*, **97**, 547–482.
- Pozo-Vázquez, D., M. J. Esteban-Parra, F. S. Rodrigo, and Y. Castro-Díez, 2001: The association between ENSO and winter atmospheric circulation and temperature in the North Atlantic region. *J. Climate*, **14**, 3408–3420.
- , S. R. Gámiz-Fortis, J. Tovar-Pescador, M. J. Esteban-Parra, and Y. Castro-Díez, 2005: North Atlantic winter SLP anomalies based on the autumn ENSO state. *J. Climate*, **18**, 97–103.
- Renwick, J. A., and J. M. Wallace, 1996: Relationships between North Pacific wintertime blocking, El Niño, and the PNA pattern. *Mon. Wea. Rev.*, **124**, 2071–2076.
- Rivière, G., and I. Orlanski, 2007: Characteristics of the Atlantic storm-track eddy activity and its relation with the North Atlantic Oscillation. *J. Atmos. Sci.*, **64**, 241–266.
- Seager, R., N. Harnik, Y. Kushnir, W. Robinson, and J. Miller, 2003: Mechanisms of hemispherically symmetric climate variability. *J. Climate*, **16**, 2960–2978.
- , Y. Kushnir, J. Nakamura, M. Ting, and N. Naik, 2010a: Northern Hemisphere winter snow anomalies: ENSO, NAO and the winter of 2009/10. *Geophys. Res. Lett.*, **37**, L14703, doi:10.1029/2010GL043830.
- , N. Naik, M. Ting, M. A. Cane, N. Harnik, and Y. Kushnir, 2010b: Adjustment of the atmospheric circulation to tropical Pacific SST anomalies: Variability of transient eddy propagation in the Pacific–North America sector. *Quart. J. Roy. Meteor. Soc.*, **136**, 277–296, doi:10.1002/qj.588.
- Simmons, A. J., and B. J. Hoskins, 1979: The downstream and upstream development of unstable baroclinic waves. *J. Atmos. Sci.*, **36**, 1239–1254.
- Smirnov, N. V., 1948: Table for estimating the goodness of fit of empirical distributions. *Ann. Math. Stat.*, **19**, 279–281.
- Smith, T. M., R. W. Reynolds, T. C. Peterson, and J. Lawrimore, 2008: Improvements to NOAA's historical merged land–ocean surface temperature analysis (1880–2006). *J. Climate*, **21**, 2283–2296.
- Straus, D., and J. Shukla, 1997: Variations of midlatitude transient dynamics associated with ENSO. *J. Atmos. Sci.*, **54**, 777–790.
- Strong, C., and G. Magnusdottir, 2008a: How Rossby wave breaking over the Pacific forces the North Atlantic Oscillation. *Geophys. Res. Lett.*, **35**, L10706, doi:10.1029/2008GL033578.
- , and —, 2008b: Tropospheric Rossby wave breaking and the NAO/NAM. *J. Atmos. Sci.*, **65**, 2861–2876.
- Thorncroft, C. D., B. J. Hoskins, and M. E. McIntyre, 1993: Two paradigms of baroclinic-wave life-cycle behavior. *Quart. J. Roy. Meteor. Soc.*, **119**, 17–55.
- Trenberth, K. E., 1981: Observed Southern Hemisphere eddy statistics at 500 mb: Frequency and spatial dependence. *J. Atmos. Sci.*, **38**, 2507–2520.
- , 1986: An assessment of the impact of transient eddies on the zonal flow during a blocking episode using localized Eliassen–Palm flux diagnostics. *J. Atmos. Sci.*, **43**, 2070–2087.
- , G. W. Branstator, D. Karoly, A. Kumar, N.-C. Lau, and C. Ropelewski, 1998: Progress during TOGA in understanding and modeling global teleconnections associated with tropical sea surface temperatures. *J. Geophys. Res.*, **103C**, 14 291–14 324.
- Vautard, R., 1990: Multiple weather regimes over the North Atlantic: Analysis of precursors and successors. *Mon. Wea. Rev.*, **118**, 2057–2081.
- Wallace, J. M., and D. S. Gutzler, 1981: Teleconnections in the geopotential height field during the Northern Hemisphere winter. *Mon. Wea. Rev.*, **109**, 784–812.
- , G. Lim, and M. L. Blackmon, 1988: Relationship between cyclone tracks, anticyclone tracks, and baroclinic waveguides. *J. Atmos. Sci.*, **45**, 439–462.
- Xue, Y., T. M. Smith, and R. W. Reynolds, 2003: Interdecadal changes of 30-yr SST normals during 1871–2000. *J. Climate*, **16**, 1601–1612.
- Zhang, Y., and I. M. Held, 1999: A linear stochastic model of a GCM's midlatitude storm tracks. *J. Atmos. Sci.*, **56**, 3416–3435.